Exploring Electronic Resonances in Pyridine: Insights from Orbital Stabilization Techniques

Maneesh Pyla¹ and Spiridoula Matsika¹

Department of Chemistry, Temple University, Philadelphia, PA, 19122, USA

(*Electronic mail: spiridoula.matsika@temple.edu)
(*Electronic mail: maneesh.pyla@temple.edu)

(Dated: 19 September 2024)

Electron attachment to pyridine results in electronic resonances, metastable states that can decay through electronic or nuclear degrees of freedom. This study uses orbital stabilization techniques combined with bound electronic structure methods, based on equation of motion coupled cluster or multi-reference methods, to calculate positions and widths of electronic resonances in pyridine that exist below 10 eV. We report four 2B_1 and four 2A_2 resonances, including one 2B_1 not previously reported experimentally and two 2A_2 resonances not reported at all in the literature. The two lower energy resonances are one-particle shape resonances while the remaining are mixed or primarily core-excited resonances. Multi-reference perturbation theory provides the best description of these resonances, especially when their character is mixed. We describe the character of these resonances qualitatively, and calculate Dyson orbitals, which provide information about their decay channels.

I. INTRODUCTION

Understanding low-energy electron attachment to cyclic conjugated molecules, like the nucleobases, may provide valuable insights into radiation-induced damage of genetic information carriers, such as DNA¹⁻⁶. Examining the impact of radiation on DNA due to interactions between electrons and molecules can in turn potentially enhance treatments for cancer and other diseases. Furthermore, these electron-induced reactions are ubiquitous and have applications beyond biology, in material science, electronics, plasmonics, and astrochemistry^{2,5,7–9}. A pivotal study by Sanche's group in 2000¹⁰ discovered that electrons below the ionization threshold have strong destructive effects, with DNA strand breaks caused by electrons having kinetic energies as low as 3 eV. In 2002, it was theoretically predicted that DNA damage can occur even through the attachment of very low energy electrons (ca. 1 eV) when DNA is strongly solvated, leading to C-O bond rupture¹¹, a finding later confirmed experimentally¹². These studies concluded that DNA damage occurs via a dissociative electron attachment (DEA) mechanism¹³, highlighting the significant impact of low-energy electrons (energy < 20 eV) on DNA and other molecules and sparking considerable scientific interest in DEA processes.

DEA is a two-step resonant process. In the first step, a lowenergy electron produced by various sources gets attached to the target neutral atom. If the resulting anion has a finite lifetime and is stable enough, it can dissociate into two or more fragments. The anions formed in the first step are known as temporary or transient negative ions or electronic resonances¹⁴. The term 'resonance' indicates that electron attachment occurs at specific energies. These electronic resonances are metastable states (with finite lifetimes) characterized by negative electron affinities.

Electronic resonances are conventionally categorized into shape and Feshbach resonances¹⁴. Shape resonances are quasi-bound states where an electron is temporarily trapped by a centrifugal potential barrier^{15,16}. This barrier restricts

the electron's motion in certain directions, trapping it within the space with molecular dimensions. The trapped electron may eventually tunnel through and escape the barrier. Shape resonances can be one-particle (1p) resonances, where in the context of the closed shell molecular systems we are discussing here, an electron is attached to a valence unoccupied orbital of the molecule. Alternatively, in 'core-excited' or '2particle-one-hole (2p-1h) resonances' an incoming electron with higher energy undergoes inelastic scattering, leaving the molecule in an electronically excited state and trapping the electron within its potential well. 2p-1h resonances can be shape or Feshbach resonances. If they lie below the parent excited state, they are termed Feshbach resonances; if they lie above the parent excited state, they are called core-excited or 2p-1h shape resonances. It is noted that the term 'coreexcited' is not limited to core electrons alone; rather, in this case it is used to denote the 2p-1h resonances. Feshbach resonances, named after the American physicist Herman Feshbach, are also known as 'Type-I resonances.' The decay of Feshbach resonances into the parent state is energetically forbidden, though decay into other states is allowed¹⁴. Feshbach resonances decay via two-electron processes leading to longer lifetimes. They are also harder to characterize theoretically, since configurations with two or more electrons rearranged are required.

Quantum mechanically, resonances can be described as stationary states with complex energies. The energy of the resonance E, also known as Siegert energy, is given by

$$E = E_r - i\Gamma/2. \tag{1}$$

The real part of the Siegert energy, E_r , is the position, while Γ is the width, where width is inversely proportional to the lifetime of the resonance ($\tau = \hbar/\Gamma$). The outcomes of the decay depend on the energy and lifetime of the resonance.

These states are not part of the Hermitian domain as their solutions and eigenvalues are derived by considering outgoing boundary conditions¹⁹, making resonances non- L^2 integrable^{16,19}. Since these resonances are embedded in

the continuum, conventional quantum chemical methods designed for solving the time-independent Schrödinger equation for bound states cannot be used without modifications^{20–23}. Alternative methods that do not require explicit continuum calculations have been developed, such as the stabilization technique^{23–31}, complex scaling^{32–34}, complex absorbing potentials^{23,35,36}, and analytic continuation in coupling constant method³⁷.

In this paper, we apply the orbital stabilization method (OSM) to compute complex energies via the analytic continuation of eigenvalues obtained from Hermitian methods 30,31,38–40. This approach, introduced by Hazi and Taylor 25,40, utilizes stabilization plots based on energies from multiple electronic states of the anion, computed using quantum chemical methods, while a parameter controlling the radial extent of added diffuse functions in the basis set is varied.

Our study focuses on pyridine (C_5H_5N), a molecule similar to benzene but with a nitrogen atom replacing a CH group. Pyridine's structural similarity to pyrimidine ($C_4H_4N_2$), a component of DNA nucleobases, makes it a suitable model for understanding how these cyclic conjugated structures interact with low-energy electrons. Thus, studying interaction of pyridine with low-energy electrons serves as a starting point for investigating relevant nucleobase molecules. On the other hand, the high symmetry present in pyridine allows for using higher levels of theory to benchmark performance.

The low-lying resonances of pyridine have been identified in electron transmission experiments^{41–44}. DEA experiments have also been reported⁴⁵. Early studies by Nenner and Schulz⁴¹ identified three low-lying resonances using electron transmission measurements. They characterized the first two as shape resonances and suspected that the third resonance was a shape mixing with a low-lying core-excited resonance. In 1976, Mathur and Hasted⁴² identified five resonances using electron transmission spectroscopy; however, they didn't characterize any of them. More recently, Szmytkowski et al⁴⁴ used linear electron-transmission method to identify resonances. A few theoretical studies have been done using scattering approaches^{46–48}. Scattering methods use different approaches to describe the target states of the neutral molecule. The static exchange (SE) approximation uses a frozen Hartree-Fock wavefunction and is incapable of describing 2p-1h resonances, while the static-exchange-polarization (SEP) approximation allows for polarization of the neutral core often including 1p1h configurations, so it can predict 2p-1h resonances, although with some deficiencies. The close coupling (CC) model uses target states obtained from the CASSCF calculations including excited states. So, the CC model is able to describe 2p-1h resonances quite well, depending on the underlying active space. 49 Barbosa et al46 used the Schwinger multichannel method with SEP to calculate the first three shape resonances, while Sieradzka et al^{47,50} used Rmatrix techniques with SEP to calculate elastic and inelastic collisions obtaining many resonances. A recent study by Su et al. 48 also used the R-matrix with close coupling and reported the two low lying $1^{2}B_{1}$, $1^{2}A_{2}$ shape resonances and the $2^{2}B_{1}$ mixed shape resonance. They also reported five core-excited

resonances 1^2A_1 , 1^2B_2 , 3^2B_1 , 2^2A_2 and 4^2B_1 above the first electronic excitation threshold. However, only the last study is able to describe both 1p and 2p-1h resonances. Furthermore, there have only been scattering approaches used to describe these resonances, so different approaches should be applied as well.

Advances in more recent years in electronic structure based approaches to calculating metastable states provide an opportunity to see how well they are applied to medium-sized molecules, such as pyridine, and compare to the available scattering results. The primary objective of our study is to determine the positions and widths of the π resonances below the ionization threshold energy (\approx 10 eV) for pyridine using high level electronic structure theory combined with the orbital stabilization technique, and to describe the nature of resonances formed by pyridine accurately. In order to achieve this goal, we implemented and used both quadratic and cubic Generalized Padé Approximant (GPA) methods to calculate resonance parameters in pyridine using OSM and compared the results with previous theoretical and experimental values.

The article is structured as follows: Section II is divided into two subsections. Section II A details the theoretical methodologies for the quadratic and cubic GPA approaches, while Section II B discusses the quantum methods and computational techniques employed in this study. Section III is dedicated to analyzing our findings, subdivided into four subsections. Section III A focuses on benchmarking basis sets. Section III B and Section III C present results obtained using single-reference and multi-reference methods, respectively. Section III D compares our results with existing literature. Finally, Section IV summarizes the conclusions drawn from our study.

II. THEORY AND COMPUTATIONAL METHODS

A. ORBITAL STABILIZATION METHOD

The core concept of the stabilization strategy involves enclosing the resonant state within an artificial box potential, where variations in the box size allow for monitoring the resonance's energy⁵¹. In the OSM, the confining potential is determined by the spatial extent of the most diffuse Gaussian functions, with the box size adjusted by varying the exponent of these functions using a scaling parameter (α). Resonance solutions are identified when the energy of the discrete state corresponding to the resonance remains invariant under changes in the scaling parameter, while the energy of the discretized continuum states increases rapidly with α .

The energies involved in avoided crossings can be analytically continued to a complex plane through GPAs^{52,53} technique to obtain Siegert complex energies. The GPAs that are used in this work are quadratic⁵⁴ and cubic polynomials which are given by,

$$E^2P + EQ + R = 0 (2)$$

$$E^{3}P + E^{2}Q + ER + S = 0 (3)$$

The coefficients P, Q, R, and S are polynomials of the scaling parameter (α) , as shown below:

$$P = 1 + \sum_{i=1}^{n_i} p_i \alpha^i$$
 $Q = \sum_{j=0}^{n_j} q_j \alpha^j$ $Q = \sum_{k=0}^{n_k} r_k \alpha^k$ $Q = \sum_{l=0}^{n_l} r_l \alpha^l$

Quadratic and cubic polynomials are denoted by (n_i, n_i, n_k) and (n_i, n_i, n_k, n_l) , respectively, and the number of unknowns in the polynomials is given by $n_i + n_j + n_k + 2$ and $n_i + n_j +$ $n_k + n_l + 3$, respectively. These polynomials are used to fit the ab initio energies as a function of the scaling parameter around avoided crossings between discrete local state and discretized continuum states. The process involves substituting these energies and scaling parameters (α) into the polynomial equations, which then transform into sets of linear equations with unknown coefficients. To calculate these unknown coefficients, a total of $n_i + n_j + n_k + 2$ and $n_i + n_j + n_k + n_l + 3$ equations are required for quadratic and cubic polynomials, respectively. These linear equations are typically solved using standard matrix methods to obtain the unknown coefficients. This process transforms GPAs into expressions involving energies and the scaling parameter (α).

The roots of the quadratic polynomial GPAs⁵⁵ are provided by

$$E_{\pm} = (-Q \pm \sqrt{(Q^2 - 4PR))}/(2P)$$
 (4)

The roots of the cubic polynomial GPAs⁵⁶ are provided by

$$E_1 = (-1/3)(Q/P) + (D+E)$$
 (5)

$$E_2 = (-1/3)(Q/P) + (1/2)(D+E) + (i/2)\sqrt{3}(D-E)$$
(6)

$$E_3 = (-1/3)(Q/P) + (1/2)(D+E) - (i/2)\sqrt{3}(D-E))$$
(7)

where

$$D = \sqrt[3]{(B+\sqrt{C})}$$
 and $E = \sqrt[3]{(B-\sqrt{C})}$

$$C = A^3 + B^2$$

$$A = \left(3RP - Q^2\right) / \left(9P^2\right)$$

$$B = \left(9PRQ - 27P^2S - 2Q^3\right) / \left(54P^3\right)$$

As the resonance energy should be independent of the scaling parameter, we utilized $\frac{dE}{d\alpha} = 0^{57}$ to locate the complex stationary points using Muller's optimization method⁵⁸. Once

these stationary points are identified, we substitute them back into the polynomial equations to extract the resonance positions from the real part and the resonance widths from the imaginary part of the complex energies.

In our study, we employed a rigorous approach to determine resonance parameters using GPAs, specifically quadratic and cubic polynomials. For each avoided crossing analyzed, we utilized at least two datasets for quadratic GPAs and three datasets for cubic GPAs. This approach was inspired by the work of Chao et al.³¹, where energies from three eigenstates (two for quadratic GPAs) near the avoided crossing were chosen for analytic continuation. All roots provided consistent results when the correct stationary point was identified. Our analysis indicated that varying α with the step sizes of 0.01, 0.02 and 0.03 does not significantly impact the resonance parameters (see Supplemental Online Material (SOM)). However, finding stationary points using cubic GPAs (e.g., (5,5,5,5) and (7,7,7,7) posed challenges when one avoided crossing was close to another of a different resonance. In such cases, careful selection of data sets that avoid nearby crossings from other resonances was crucial. In general, a stationary point is trustworthy when the values are reproduced with all GPAs applied. In cases that is not true, we will discuss the justification for our choice.

B. COMPUTATIONAL METHODS

The geometry of neutral pyridine was optimized at the B3LYP level of theory with Dunning's correlation-consistent polarized valence triple zeta (cc-pVTZ) basis set. Different basis sets were benchmarked using the Equation of Motion Electron Attachment Coupled Cluster with Single and Double Excitations (EOM-EA-CCSD) method to identify a balance between accuracy and computational efficiency. All the basis sets were taken from the Basis Set Exchange library⁵⁹. Using the Dunning basis sets cc-pVDZ, aug-cc-pVDZ, ccpVTZ, and aug-cc-pVTZ, we added extra diffuse functions, designated with a bracket in Table I. To properly analyze anions, very diffuse orbitals are imperative, and consequently, we added additional diffuse orbitals for the heavy atoms (C and N). We also tested addition of the diffuse functions at the center of mass (COM) of the molecule. Finally, a Pople basis set was also tested. Extra diffuse basis functions are scaled in an even-tempered manner and listed in brackets in Table I. In order to check the performance of basis sets without extra functions, we also used the aug-cc-pVDZ set, and uniformly scaled all the augmented diffuse functions. All these basis sets shown in Table I were used for benchmarking.

Based on benchmarking discussed in Section III A, the ccpVTZ basis set with an additional diffuse 'p' function on heavy atoms was chosen for the remaining calculations. Stabilization curves were generated by scaling one extra diffuse 'p' function on heavy atoms while keeping the parent basis unchanged on hydrogen atoms, and exponential factors were adjusted in an even-tempered manner,

$$\alpha_{(d)} = 0.5 * \alpha_p \tag{8}$$

where $\alpha_{(d)}$ is the exponential scaling factor of the extra added diffuse function and α_p is the exponential scaling factor of the last primitive Gaussian of desired angular function in the existing basis set.

To determine the resonance parameters E_r and Γ for pyridine, orbital stabilization plots were generated using two distinct computational methods tailored to different types of resonances. The EOM-EA-CCSD method^{60,61}, part of the EOM-CCSD family, was employed for describing one particle (1p) shape resonances of pyridine. This method accurately describes electron affinities when coupled with appropriate basis sets.

However, EOM-EA-CCSD cannot adequately describe 2p-1h resonances. This is because 2p-1h resonances require double excitations which are not included in the primary space of EOM-EA-CCSD, limiting its applicability to these resonances. Going beyond EOM-EA-CCSD by including triple excitations, using EOM-EA-CCSDT, would help improve the description of 2p1h resonances, but this is a very expensive approach. 62 For this reason, multi-reference methods 63,64 have been employed instead here to describe the 2p-1h resonances. These methods offer a more comprehensive treatment of electron correlation effects and are better equipped to capture the nuances of multi-particle excitations. These methods, implemented with the same basis set, are capable of accurately calculating 2p-1h resonances by allowing a more flexible configuration space. This dual-method approach ensured comprehensive coverage of both 1p and 2p-1h resonances in pyridine, contributing to a thorough understanding of its electronmolecule interactions.

Both Complete Active Space Self-Consistent Field (CASSCF) and Restricted Active Space Self-Consistent Field (RASSCF) approaches were used. In all cases, 9 electrons were included in the active space. The orbitals included in the active space for 2B_1 and 2A_2 resonances are provided in Table II. In RASSCF, the complete active space (ACT) included the 3π and $3\pi^*$ orbitals and the lone pair on nitrogen (with symmetries 1 a_1 , 4 b_1 , and 2 a_2 , see Figure 1). Additional diffuse functions are needed to include continuum-like states and be able to describe the resonances properly. In RASSCF, we assume that the description of these additional states does not require a high level of correlation, so we include additional diffuse orbitals in the auxiliary space (AUX) and only allow single excitations into that space. The AUX space is different for the ${}^{2}B_{1}$ and ${}^{2}A_{2}$ resonances to capture coupling with the continuum states of appropriate symmetry. For ${}^{2}B_{1}$ resonances at the RASSCF level, ten diffuse orbitals of b_1 symmetry are included in the AUX space (Table II). The energies of the excited ${}^{2}B_{1}$ states were calculated including 15 states in an average of states RASSCF. The neutral reference was also calculated using the same active space and number of states to achieve balance. For ${}^{2}A_{2}$ resonances at the RASSCF level, four a_{2} diffuse orbitals are included in addition to seven valence orbitals with restricted single excitations into the AUX space (Table II). The energies of the ${}^{2}A_{2}$ resonances and the neutral reference were calculated using an average of over 10 states.

The CASSCF method was employed to assess the impact

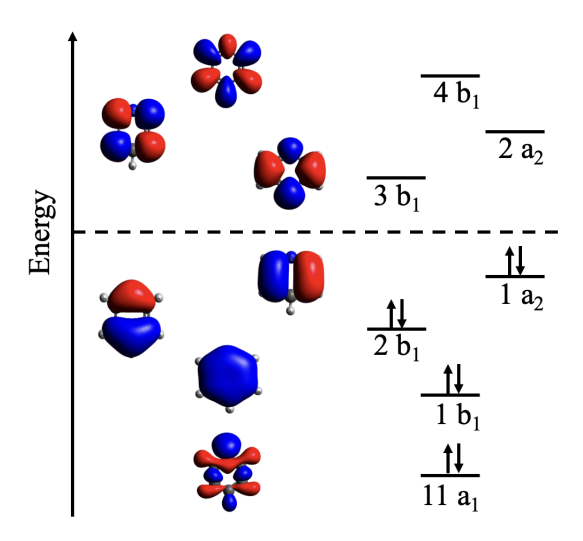


FIG. 1. Active orbitals of neutral pyridine molecule. Symmetry labels are given according to the $C_{2\nu}$ point group.

of including higher excitations into the diffuse orbitals and to determine if it affects the resonance positions and widths. At the CASSCF level, we used active spaces without restrictions for calculating the resonances of different symmetries. The energies of the excited states were calculated using an average of 10 states for both symmetries. Similarly, neutral reference has been calculated using the same active spaces with the states averaged over 10 states.

Finally, dynamical correlation was added using perturbation theory to correct the CASSCF energies and wavefunctions. Specifically, the extended multistate complete active space perturbation theory (XMS-CASPT2) approach was used with 10 states for 2B_1 and 10 states for 2A_2 states. The Ionization Potential Electron Affinity (IPEA) shift operator was used with a value of 0.25 a.u., to correct the systematic errors that associated with open shell systems and IMAGINARY shift was used with a value of 0.20 a.u. to avoid the singularities that cause intruder state problems. To calculate possible detachment channels, different symmetries of states of neutral pyridine were utilized to determine Dyson orbitals, using the same active space for both neutral and anionic states. Dyson intensities for the transitions between neutral and resonance states are provided in the SOM.

Geometry optimizations using B3LYP were performed using the Gaussian software⁶⁵. All EOM-EA-CCSD calculations were executed using Q-Chem⁶⁶. All the MCSCF calculations were carried out using the Molpro software⁶⁷, while the XMS-CASPT2 calculations and Dyson orbitals were carried out using the OpenMolcas software⁶⁸.

III. RESULTS AND DISCUSSION

The electronic configuration of the ground state of neutral pyridine molecule is shown in Figure 1, indicating the occupation of the valence π , π^* , and lone pair orbitals. Since pyridine has three π bonds and one lone pair on the nitrogen atom,

Basis set	$B_1(E_r)$	$B_1(\Gamma)$	$A_2(E_r)$	$A_2(\Gamma)$	# bfs
cc-pVDZ+[1p]	1.64	(0.10)	1.72	(0.16)	127
cc-pVDZ+[2s4p]	1.36	(0.08)	1.69	(0.08)	193
aug-cc-pVDZ	1.36	(0.05)	1.65	(0.05)	183
aug-cc-pVDZ+[1p]	1.22	(0.10)	1.54	(0.09)	201
cc-pVTZ+[1p]	1.20	(0.06)	1.50	(0.11)	268
cc-pVTZ+[2s3p]	1.13	(0.05)	1.50	(0.04)	316
cc-pVTZ+[3s3p]	1.15	(0.04)	1.50	(0.04)	322
cc-pVTZ+[2s4p]	1.13	(0.06)	1.49	(0.06)	334
cc-pVTZ+[3s4p]	1.13	(0.06)	1.48	(0.07)	340
aug-cc-pVTZ+[1p]	1.06	(0.08)	1.41	(0.08)	409
6-311G(2df,2pd)+[1p]	1.30	(0.06)	1.52	(0.11)	274
cc-pVDZ(H) cc-pVTZ+[3s3p3d]	1.08	(0.07)	1.45	(0.06)	367
cc-pVTZ+[3s3p3d] (COM)	1.29	(0.06)	1.68	(0)	277
cc-pVTZ+[6s6p6d] (COM)	1.26	(0.03)	1.66	(0.01)	304
exp. ^{41–44}	0.6-0.8		1.2		

TABLE I. Positions (E_r) and widths (Γ) (in eV) of low-lying shape resonances of pyridine obtained using EOM-EA-CCSD with different basis sets. In the last two rows, extra diffuse functions are only added at the center of mass (COM).

$C_{2\nu}$	CLOSED	ACT	AUX						
$^{2}B_{1}$ resonances									
RASSCF									
a_1	a_1 10 1								
b_1	0	4	10						
b_2	7	0	0						
a_2	0	2	0						
	CASSCF								
a_1	10	1							
b_1	0	10							
b_2	7	0							
a_2	0	2							
	² A ₂ resonances								
	RAS	SSCF							
a_1	10	1	0						
b_1	0	4	0						
b_2	7	0	0						
a_2	0	2	4						
CASSCF									
a_1	10	1							
b_1	0	4							
b_2	7	0							
a_2	0	6							

TABLE II. Orbitals included in the calculation of 2B_1 and 2A_2 resonances of pyridine at the RASSCF and CASSCF level of theory (with cc-pVTZ +[1p] basis set). The number of closed shells (CLOSED), active (ACT), and auxiliary (AUX) orbitals are shown belonging to the irreducible representations of $C_{2\nu}$ symmetry (a_1,b_1,b_2,a_2) .

there exist three occupied π orbitals, one occupied lone pair orbital, and three unoccupied π^* orbitals. The $C_{2\nu}$ symmetry of pyridine defines its orbital configurations with π and π^* orbitals belonging to b_1 and a_2 irreducible representations. Two of the occupied π orbitals have b_1 symmetry (1 b_1 and 2 b_1) while the other occupied π orbital belongs to a_2 symmetry (1 a_2). Similarly, two of the unoccupied π^* orbitals belong to b_1 symmetry, and the other belongs to a_2 symmetry. Therefore, we expect to have a maximum of three low-lying π 1p

shape resonances and several 2p-1h resonances. The 1p shape resonances are formed by electron attachment to a π^* orbital, while the 2p-1h involve excitation from π to π^* and attachment of an electron to a π^* orbital.

In this work, our objective is to characterize many of the B_1 and A_2 resonances of pyridine that exist below 10 eV. To choose an accurate as well as cost-efficient basis set, we initially benchmark some basis sets using the single reference EOM-EA-CCSD method for the first two low-lying resonances in Section III A.

A. BENCHMARKING DIFFERENT BASIS SETS

In order to benchmark the basis sets we calculated the first shape ${}^{2}B_{1}$ and ${}^{2}A_{2}$ resonances and compared to experimental values. Benchmarking of basis sets was done only using the 1p resonances in this work. In the future, we plan to examine whether 2p-1h resonances have different requirements for basis sets. In this work this is not possible, since we do not have available experimental results for the 2p-1h resonances of pyridine. The results obtained for different basis sets beginning from cc-pVDZ+[1p] to aug-cc-pVTZ+[1p] at the EOM-CCSD level are presented below in Table I. The results for basis sets using diffuse functions at the COM are provided in the same table (last two rows) for comparison with the ones that add diffuse functions on all heavy atoms. In the table, the parent basis set is not modified on hydrogen atoms unless it is mentioned in parenthesis. All the stabilization plots are provided in the SOM, and the values reported in Table I are average of all the values that are obtained across all the avoided crossings for a given resonance using quadratic GPA.

The variation in resonance parameters for the basis sets (excluding the last four rows) is provided in Figure 2 for a more visual representation. The positions decrease with an increase in the number of basis functions approaching some convergence, while the widths are in a similar range between 0.04-0.16 eV, except for cc-pVDZ+[1p], and they show no

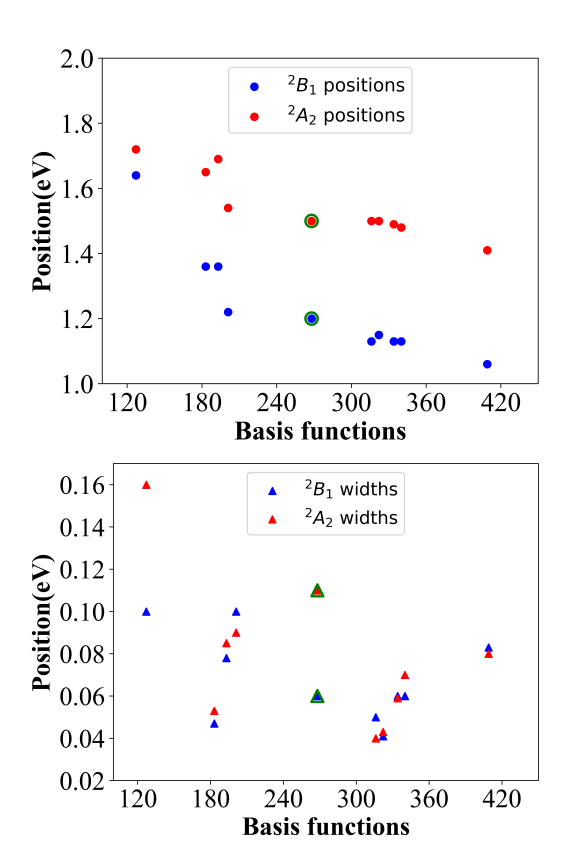


FIG. 2. Resonance positions (top) and widths (bottom) vs number of basis functions shown in Table I for both 2B_1 and 2A_2 resonances. Marked dots belong to cc-pVTZ+[1p]. Values are obtained using (7,7,7) GPA. Basis sets from cc-pVDZ+[1p] to aug-cc-pVTZ+[1p] added on all heavy atoms are used to see the variation across the same correlation consistent basis set family.

systematic convergence. Among all the atom-centered basis sets, cc-pVDZ+[1p] has the lowest number of basis functions (127) and aug-cc-pVTZ+[1p] has the highest number of basis functions (409). The experimental values for the 1^2B_1 and 1^2A_2 positions are around 0.7 eV and 1.2 eV. All the basis sets predict higher values. The values obtained using cc-pVDZ in Table I are too high even when diffuse functions are added, indicating the necessity of using larger basis sets. The values obtained at aug-cc-pVDZ+[1p] and cc-pVTZ+[1p] seem to balance best accuracy with computational efficiency compared to the remaining larger basis sets. The error is still 0.5 eV for 1^2B_1 and 0.3 eV for 1^2A_2 . Beyond the ccpVTZ+[1p] basis set, the marginal increase in accuracy with additional basis functions suggests limited potential for improvement with larger basis sets. Expanding the basis set with more diffuse functions introduces additional 'continuum-like' functions below the desired states. This augmentation necessitates calculations of more excited states, thereby increasing the overall computational time both because of the number of basis functions and because of the increased number of roots that need to be converged.

While the best position is obtained with the largest basis set, aug-cc-pVTZ+[1p], (with an error of 0.3-0.5 eV and 0.2

eV for 1^2B_1 and 1^2A_2 , respectively, compared to experimental values), the next best value is obtained using a basis set that combines smaller basis sets for lighter atoms and larger basis sets for heavier atoms (e.g., cc-pVDZ(H) for lighter atoms and cc-pVTZ+[3s3p3d] for heavier atoms). This approach is one way to reduce the number of basis functions without sacrificing accuracy. We also conducted a comparison between Dunning's basis set and Pople's basis set to evaluate their reliability in correlation calculations. Specifically, we selected a basis set (6-311G(2df,2pd)+[1p]) that has a comparable number of basis functions (274) to cc-pVTZ+[1p] (268). Our findings revealed that the resonance positions obtained with Pople's basis set were higher compared to those obtained with Dunning's basis sets, while the widths remained similar. This suggests that Dunning's basis sets perform better than Pople's basis set in resonance calculations.

To compare the resonance parameters obtained by adding diffuse functions only at the center of mass (COM) with the ones with atom-centered basis, we considered two different basis sets, cc-pVTZ+[3s3p3d] and cc-pVTZ+[6s6p6d], which have 277 and 304 basis functions, respectively. The positions obtained are larger than the ones with atom-centered cc-pVTZ+[1p]. For 1^2B_1 resonances, the calculated widths were comparable to those obtained with atom-centered basis sets, whereas reasonable widths for 1^2A_2 resonances were not achieved.

Based on our benchmarking, the aug-cc-pVDZ+[1p] and cc-pVTZ+[1p] basis sets strike the best balance between accuracy and efficiency. The positions are very similar when using these basis sets, but the widths seem to be a little better with cc-pVTZ+[1p]. For this reason, we chose cc-pVTZ+[1p] for all subsequent calculations in this work, even though it is somewhat larger than aug-cc-pVDZ+[1p].

B. SHAPE RESONANCES USING EOM-EA-CCSD

EOM-EA-CCSD calculations were conducted using the cc-pVTZ+[1p] basis set, and were used to obtain results for the shape resonances of pyridine. The stabilization curves for 2B_1 and 2A_2 states are depicted in Figure 3. Resonance positions and widths for 2B_1 and 2A_2 states are summarized in Table III. The calculations utilized quadratic-(7,7,7), cubic-(5,5,5,5), and cubic-(7,7,7,7) GPAs to determine the resonance parameters.

GPA	1^2B_1	1^2A_2	2^2B_1
(7,7,7)			6.02 (0.39)
			5.91 (0.31)
(7,7,7,7)	1.19 (0.06)	1.49 (0.08)	5.96 (0.30)
Average	1.19 (0.05)	1.49 (0.09)	5.96 (0.34)

TABLE III. Positions and widths (in parenthesis) obtained using EOM-EA-CCSD/cc-pVTZ+[1p] for 2B_1 and 2A_2 shape resonances (in eV). (5,5,5,5) GPA values for 1 2A_2 are excluded from the average as the width is not consistent with the remaining two GPAs.

Two ${}^{2}B_{1}$ shape resonances were identified corresponding to the shape resonances with the electron attached to the $3b_{1}$ or

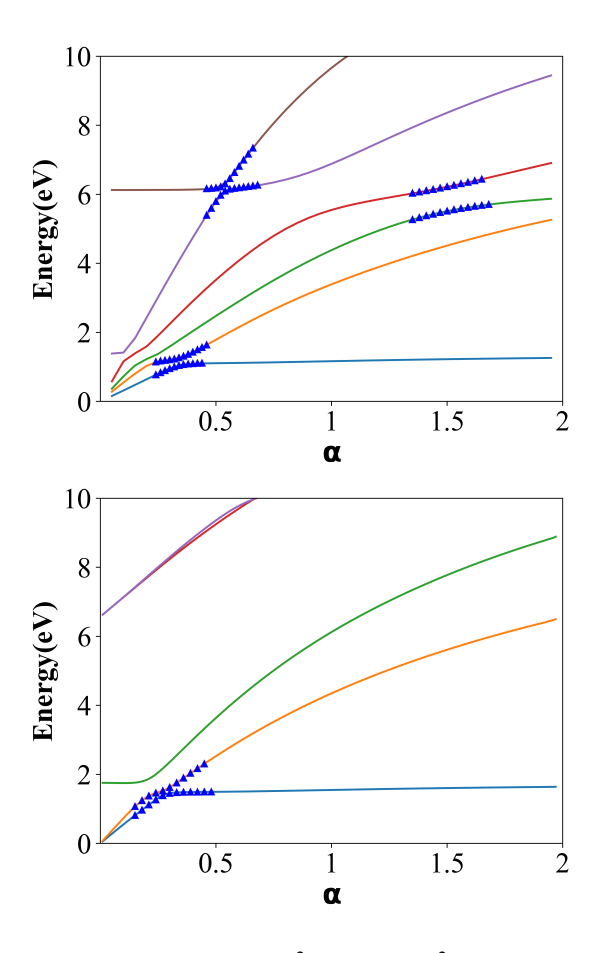


FIG. 3. Stabilization curves for 2B_1 (top) and 2A_2 (bottom) states obtained from EOM-EA-CCSD/cc-pVTZ+[1p]. Avoided crossings used in the quadratic-GPA are highlighted with blue triangles.

 $4b_1$ orbitals. We used one avoided crossing corresponding to the first ${}^{2}B_{1}$ resonance, shown in Figure 3. The positions and widths for both quadratic and cubic GPAs are similar. The position of 1^2B_1 is at 1.2 eV, while the width 0.05 eV, corresponding to a lifetime of 83 fs. The second ${}^{2}B_{1}$ resonance, $2^{2}B_{1}$, has two avoided crossings occurring at α values around 0.53 and 1.5, respectively. The values in Table III are average values obtained from these two avoided crossings. Consistent across all GPAs, the widths for the second ${}^{2}B_{1}$ resonance are larger compared to the first, and widths obtained at larger α values are greater than those at smaller α values (see SOM). The problem of avoided crossings giving different widths for the same resonance is well known in OSM, and it has been attributed to contributions of different partial widths. Recently, Jordan and coworkers have proposed a way to extract partial widths from stabilization curves⁶⁹. The position for 2^2B_1 resonance using the average values of the two avoided crossings is predicted to be around 6 eV. The width for the higher energy resonance is expected to be larger, corresponding to a shorter-lived state, and it is indeed predicted to be 0.3 eV, for a lifetime of just 14 fs.

As expected, 1^2A_2 resonance is captured with EOM-EA-CCSD, corresponding to the shape resonance with the electron attached to the a_2 orbital. The corresponding avoided cross-

ing is highlighted in the stabilization curves in Figure 3. The widths obtained with cubic-(5,5,5,5) differ significantly from the other two GPAs. However, the positions and widths obtained with quadratic-(7,7,7) and cubic-(7,7,7,7) match well with reported values in the literature (see Table III). For this reason, we excluded the (5,5,5,5) from the average. These discrepancies suggest that the number of data points used around the avoided crossing is crucial for identifying the correct stationary point. The 1^2A_2 resonance is predicted to be 0.3 eV above 1^2B_1 , and the width is twice as large, 0.1 eV, giving a lifetime of 41 fs.

The resonance parameters obtained for all three resonances using quadratic and cubic GPAs are very similar, suggesting that cubic GPA can be reliably used to calculate resonance parameters.

C. RESONANCES USING MULTI-REFERENCE METHODS

While EOM-EA-CCSD provides good estimates for positions and widths, it is not able to capture all reported resonances. It is suitable for describing 1p resonances but inadequate for 2p-1h processes, and does not account for mixing between different characters. This indicates the need for a more comprehensive theory to accurately describe resonances. Therefore, to gain deeper insights into the nature of pyridine resonances, we employed multi-reference methods, CASSCF, RASSCF, and XMS-CASPT2 using the ccpVTZ+[1p] basis set. We also performed a comparative analysis of CASSCF vs RASSCF to balance computational cost and accuracy in our resonance calculations. We used these methods to perform orbital stabilization calculations. Resonance parameters were determined using quadratic and cubic GPAs, and stabilization plots for B_1 resonances are shown in Figure 4, while plots for A_2 resonances are presented in Figure 5.

1. ${}^{2}B_{1}$ Resonances

Stabilization plots for 2B_1 resonances at the RASSCF, CASSCF and XMS-CASPT2 levels are shown in Figure 4. Unlike EOM-EA-CCSD, there are four resonances that are present with these methods. The resonance parameters using various GPAs are provided in SOM, along with more detailed discussion on which avoided crossings were used. The average final results are given in Table IV (positions) and Table V (widths).

The stabilization plots for RASSCF and CASSCF are comparable, resulting in similar avoided crossings and positions and widths. The positions in some cases may differ by up to 0.2 eV, but most of the time they are very similar. In addition, the widths are very similar between the two approaches. This validates our hypothesis and shows that using RASSCF, where diffuse orbitals are included in the auxillary space to reduce the computational cost, is a valid approach. For both of these methods we were not able to obtain values for the

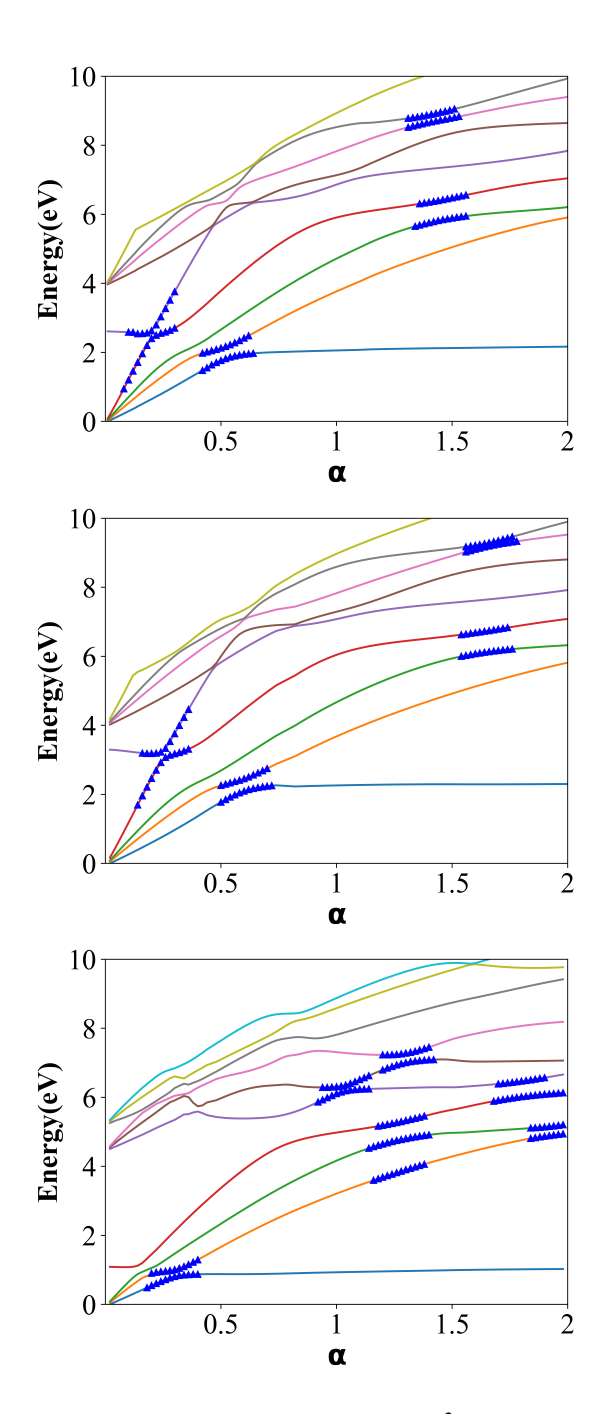


FIG. 4. Stabilization graphs for pyridine 2B_1 resonances at RASSCF/cc-pVTZ + [1p] (top), CASSCF(9,13)/cc-pVTZ + [1p] (middle) and XMS-CASPT2 (bottom) levels. Avoided crossings used in the quadratic-GPA are highlighted with blue triangles. The energies in the stabilization plots are provided by taking first point as a reference ($\alpha = 0.02$).

third ${}^{2}B_{1}$ resonance, because there are several avoided crossings between the resonances themselves.

Adding perturbation theory corrections with XMS-CASPT2 leads to better avoided crossings, so we were able to obtain values for all four resonances. XMS-CASPT2 stabilizes all the positions by 1 eV or more, except 2^2B_1 which

is stabilized by 0.6 eV compared to CASSCF. This shows the importance of dynamical correlation. Similarly, all the widths become smaller at the XMS-CASPT2 level, except for that of 2^2B_1 .

The resonance positions for 1^2B_1 calculated with CASSCF and RASSCF are greater than the values reported in the literature. This arises from the difficulty in obtaining a balanced description between the neutral and the anion, because of the differential correlation, which leads to an overestimation of electron attachment values. XMS-CASPT2 behaves in a much better way, and predicts the first resonance at a similar position as EOM-EA-CCSD and as some of the scattering results, although still higher than experiment. However, the positions obtained for 2^2B_1 resonance are lower than the EOM-EA-CCSD values and more in agreement with experiment. This will be discussed in more detail in Section III D.

Table IV and Table V also show the uncertainties in the values. Uncertainties are calculated because we used several GPA, and some times several avoided crossings, to determine the positions and widths. So we can calculate the average and the standard deviation from these values. As can be seen in the table, in some cases the uncertainty is great. The largest uncertainty is for the 1^2B_1 position at the CASSCF level, which is 0.4 eV. This is because there are several avoided crossings interacting with each other, making the analysis quite challenging. On the other hand, the uncertainty at the XMS-CASPT2 level is only 0.01 eV. Uncertainties for the other resonances are always less than 0.1 eV. Uncertainties for widths are also less than 0.1 eV in most cases, although this is a larger percentage of the actual value for widths.

2. ²A₂ Resonances

The stabilization curves for 2A_2 resonances are shown in Figure 5, while the results from all the GPA used are shown in SOM. Average final results are shown in Table IV and Table V. We were able to locate four 2A_2 resonances below 10 eV. The position of the first one, $1{}^2A_2$, at the CASSCF and RASSCF levels is at 2.6 eV, only 0.3 eV above $1{}^2B_1$. The other resonances are at higher energies, at 7.9 eV, 8.7 eV, and 9.5 eV. The width of $1{}^2A_2$ at the CASSCF/RASSCF levels is 0.2 eV, while the widths of the other resonances are much smaller, between 0.01- 0.07 eV.

Similarly to the 2B_1 resonances, the RASSCF and CASSCF results agree very well, suggesting that using RASSCF is the best approach. Widths for these higher resonances are smaller than those for the first 2A_2 resonance, suggesting much longer lifetimes.

XMS-CASPT2 stabilizes the positions by 1 eV or more, similar stabilization that was seen for 2B_1 resonances. The width of 1^2A_2 is predicted to be 0.09 eV, smaller than that at the CASSCF level. The widths for the higher 2A_2 resonances are also smaller when adding correlation through perturbation theory.

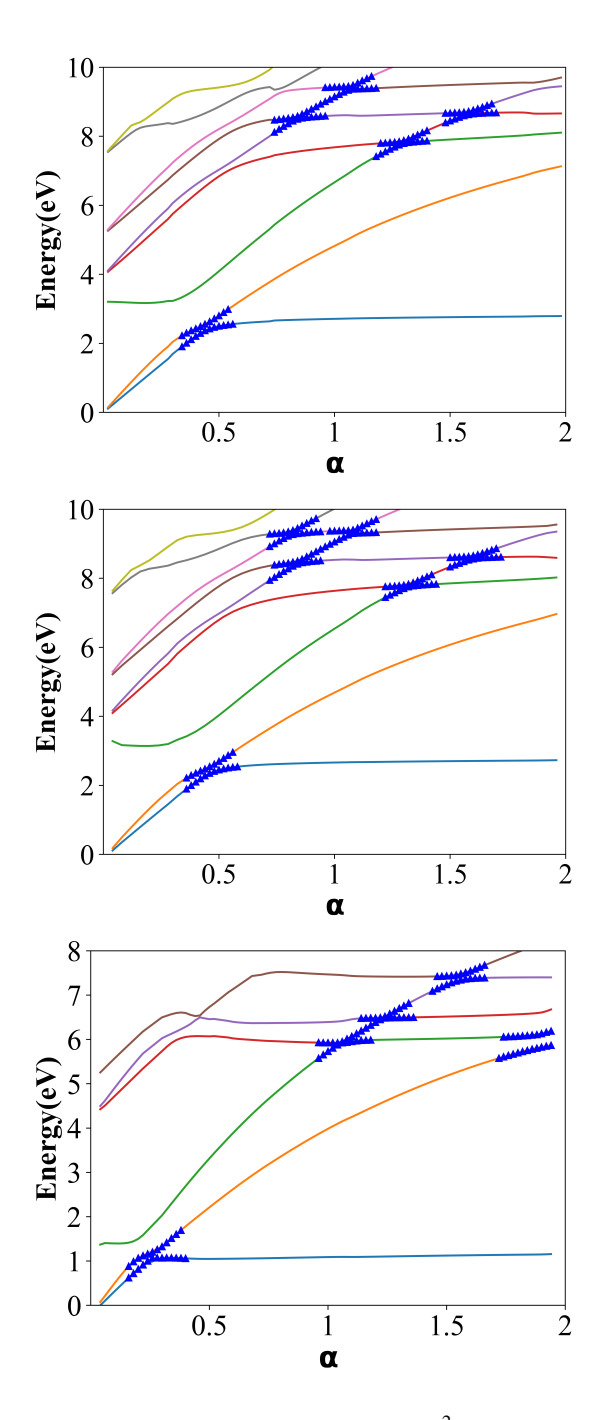


FIG. 5. Stabilization graphs for pyridine 2A_2 resonances at RASSCF/cc-pVTZ+[1p] (top), CASSCF(9,11)/cc-pVTZ+[1p] (middle) and XMS-CASPT2 (bottom) levels. Avoided crossings used in the quadratic-GPA are highlighted with blue triangles. The energies in the stabilization plots are provided by taking first point as a reference ($\alpha=0.02$)

3. Character of resonances and decay channels

To investigate the nature of the resonances, we analyzed the wavefunctions at the CASSCF and XMS-CASPT2 levels using the stable part of the stabilization curves, where it is easier to attribute the wavefunction to the resonances rather than the

pseudocontinuum states. Extracting wavefunctions from the stable part of the wavefunctions has been used before to calculate properties, such as transition dipole moments⁷⁰. The configurations with contributions > 0.3 for the 2B_1 resonances are provided in Figure 6, and for 2A_2 resonances in Figure 7. Occupation numbers from natural orbitals are also provided for a better assessment of the character. Results from CASSCF are shown, because the occupation numbers showed less mixing with the continuum states.

The first 1^2B_1 resonance is predominantly a 1p resonance with attachment of the electron at the $3b_1$ orbital (coefficient: 0.94). The 2^2B_1 resonance also has primarily 1p resonance, but with a significant 2p-1h component, indicating a mixed nature. The occupation numbers confirm the mixing. The 3^2B_1 resonance is dominated by 2p-1h configuration, with contributions from multiple configurations. 4^2B_1 is also a core-excited resonance with several contributions. There are three common configurations that contribute to all three 2^2B_1 , 3^2B_1 and 4^2B_1 resonances, with different mixings.

We also explored the nature of the 2A_2 resonances. Details of all major configurations (contributions greater than 0.3) are provided in Figure 7. The first 2A_2 resonance is entirely dominated by the 1p shape configuration, with a coefficient of 0.95. The 2^2A_2 resonance is primarily dominated by a 2p-1h configuration, but also involves excitations from a_2 to b_1 orbitals leading to three unpaired electrons. The third and fourth 2A_2 resonances also exhibit significant contributions from several configurations with core-excited character.

Overall there is significant mixing of configurations in the higher resonances, which leads us to the important question of the channels in which these resonances can decay. In order to explore these channels we calculated the neutral A_1 and B_2 excited states, and the Dyson orbitals connecting the anion with the neutral states. Dyson orbitals are calculated by integrating the overlap of the neutral and anion states resulting in a one electron function (orbital), which represents the attached electron. Dyson orbitals for resonances have been implemented using the complex absorbing potentials approach before⁷¹. These states arise by excitation of an electron from either $2b_1$ or $1a_2$ occupied orbitals to either $3b_1$ or $2a_2$ unoccupied orbitals. This leads to four configurations (without considering spin), two of which have A_1 symmetry $(2b_1 \rightarrow 3b_1,$ $1a_2 \rightarrow 2a_2$) and two B_2 symmetry $(2b_1 \rightarrow 2a_2, 1a_2 \rightarrow 3b_1)$. It turns out the electronic states are a mixing of the configurations of the same symmetry, shown in Figure 8. Section III D shows the energies of the neutral states and the resonances. This diagram shows that the resonances are core-excited shape resonances rather than Feshbach resonances, since many of the triplet neutral states are below the resonances, so the resonances can decay to these states via an one electron detachment.

In order to see better where they decay we calculated the Dyson norms between resonances and neutral states. We chose an α value where the stabilization is stable so that we have a good representation of the resonance wavefunction. Table 8 in SOM shows the Dyson norms between the resonances and the neutral states. The 1^2B_1 1p shape resonance has the largest Dyson norm with the ground state, since removal of

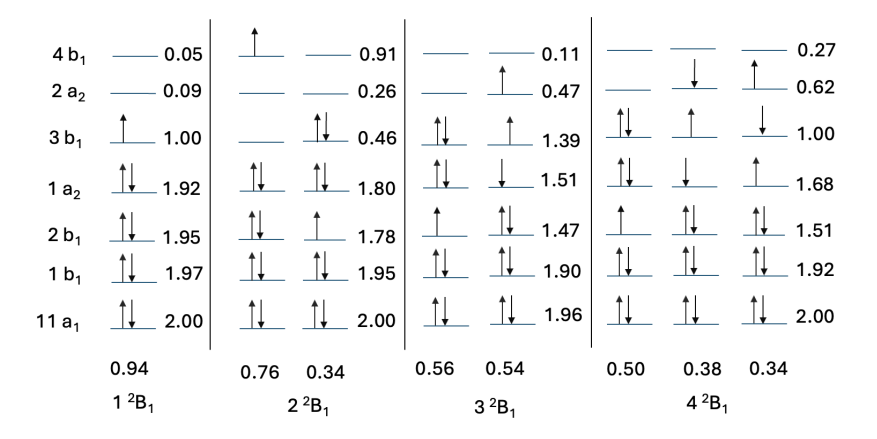


FIG. 6. Major configurations that are contributing to all the ${}^{2}B_{1}$ resonances at CASSCF level of theory. Configurations for $3{}^{2}B_{1}$ are taken from CASPT2. The coefficients of the corresponding configurations in the wavefunction are given at the bottom. Occupation numbers from natural orbitals are shown on the right side.

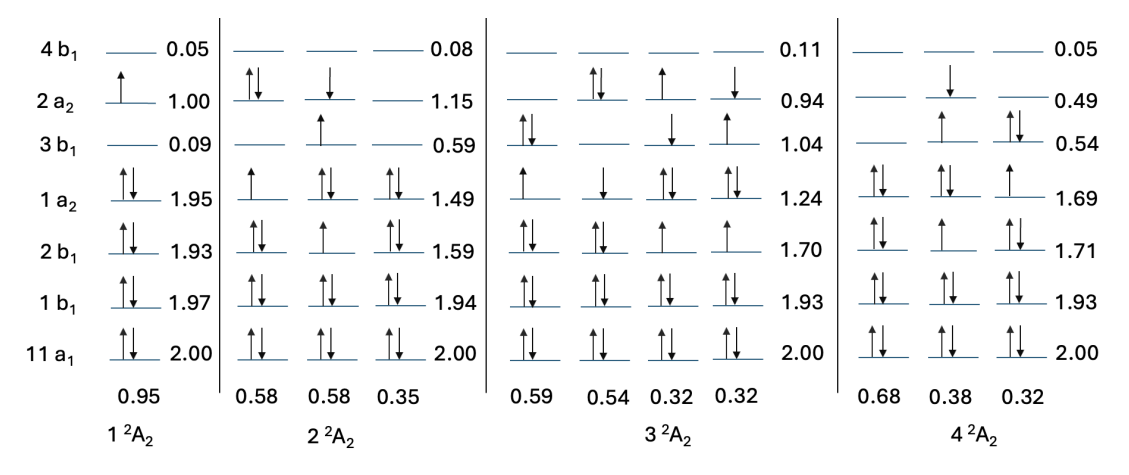


FIG. 7. Major configurations that are contributing for all the ${}^{2}A_{2}$ resonances at CASSCF level of theory. The coefficients of the corresponding configurations in the wavefunction are given at the bottom. Occupation numbers from natural orbitals are shown on the right side.

the unpaired electron can lead to the closed shell ground state, which is the dominant decay channel. The other Dyson norms are significant as well, since removal of electrons from lower orbitals can lead to excited neutral states, but this decay is energetically not possible. 2^2B_1 can decay to the ground state, as well, by removal of the electron from the $4b_1$ orbital, but it can also decay to the 2^3A_1 state by removal of an electron from the $3b_1$ orbital. Interestingly, even though both 1^3A_1 and 2^3A_1 have contributions from similar configurations, this resonance has a significant Dyson norm only with 2^3A_1 . This highlights the importance of calculating the Dyson norms. The 3^2B_1 resonance can decay primarily to 1^3A_1 by detachment of an electron from the $3b_1$ orbital. 4^2B_1 similarly can decay to 2^3A_1 , 1^3B_2 and 1^1B_2 .

Dyson norms connecting the ${}^{2}A_{2}$ resonances to the neutral states are shown in Table 9 in SOM. Again, the 1p resonance $1{}^{2}A_{2}$ has the largest Dyson norm with the ground state, but also substantial norms with the other states. $2{}^{2}A_{2}$ can decay to $1{}^{3}A_{1}$ primarily while $3{}^{2}A_{2}$ and $4{}^{2}A_{2}$ decay to $2{}^{3}A_{1}$ and $1{}^{3}B_{2}$.

Overall, this analysis of Dyson norms shows that the resonances can decay to several channels, although it is not always

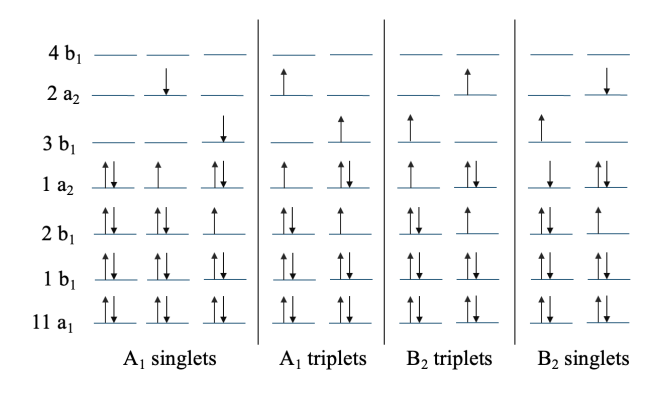


FIG. 8. Configurations of neutral states in which the resonances can decay

clear which ones without calculating the Dyson orbitals and their norms.

Method/Lit	$1^{2}B_{1}$	$1^{2}A_{2}$	$2^{2}B_{1}$	$2^{2}A_{2}$	$3^{2}B_{1}$	$3^{2}A_{2}$	$4^{2}B_{1}$	$4^{2}A_{2}$
Nenner and Schulz (exp) ⁴¹	0.62	1.20	4.58	-	-	-	-	-
Modelli and Burrow (exp) ⁴³	0.72	1.18	4.48	-	-	-	-	-
Szmytkowski et al. (exp) ⁴⁴	0.7	1.20	4.6	-	-	-	-	-
Mathur and Hasted (exp) ⁴²	0.79	1.15	4.71	-	-	-	7.27	7.86
Barbosa et al. ⁴⁶	0.90	1.33	5.80	-	-	-	-	-
Su et al. ⁴⁸	0.83	1.08	5.67	6.95	6.38	-	7.26	-
Sieradzka et al. ⁴⁷	0.67	1.07	5.33	-	-	-	-	-
EOM-EA-CCSD	1.19	1.49 ± 0.01	5.96 ± 0.21	-	-	-	-	-
RASSCF	2.29 ± 0.22	2.60 ± 0.01	6.19 ± 0.01	7.94	-	8.72 ± 0.07	8.76 ± 0.04	9.55
CASSCF	2.32 ± 0.38	2.62 ± 0.03	6.06 ± 0.01	7.82	-	8.57 ± 0.07	8.79 ± 0.04	9.38 ± 0.04
XMS-CASPT2	1.32 ± 0.01	1.66 ± 0.02	5.42 ± 0.01	6.51 ± 0.06	6.60 ± 0.02	7.00 ± 0.00	7.46 ± 0.00	7.91 ± 0.00

TABLE IV. Positions (in eV) of all the resonances found in this work, and comparison with selected experimental and theoretical studies reported in the literature. Average values from the various GPAs and avoided crossings are given, along with the standard deviation.

Method/Lit	$1^{2}B_{1}$	$1^{2}A_{2}$	$ 2 ^{2}B_{1}$	$ 2 ^2A_2$	$3^{2}B_{1}$	$3^{2}A_{2}$	$4^{2}B_{1}$	$4^{2}A_{2}$
Su et al. ⁴⁸	0.05	0.04	0.35	0.22	-	-	0.21	-
Sieradzka et al. ⁴⁷	0.03	0.03	0.47	-	-	-	-	-
EOM-EA-CCSD	0.05 ± 0.01	0.09 ± 0.01	0.34 ± 0.29	-	-	-	-	-
RASSCF	0.13 ± 0.07	0.17 ± 0.06	0.26 ± 0.06	0.07	-	0.06 ± 0.01	0.45 ± 0.01	0.01 ± 0.00
CASSCF	0.16 ± 0.08	0.25 ± 0.01	0.23 ± 0.04	0.06	-	0.06 ± 0.02	0.25 ± 0.13	0.04 ± 0.03
XMS-CASPT2	0.06 ± 0.01	0.09 ± 0.01	0.28 ± 0.12	0.05 ± 0.03	0.14 ± 0.10	0.01 ± 0.00	0.06 ± 0.00	0.02 ± 0.00

TABLE V. Widths (in eV) of all the resonances found in this work, and comparison with selected experimental and theoretical studies (in eV) reported in the literature. Average values from the various GPAs and avoided crossings are given, along with the standard deviation.

D. COMPARISONS WITH LITERATURE

We will now make a more detailed comparison between our results and previous theoretical and experimental studies. Table IV shows the position from previous work and our calculated results from all the methods used in this work. Most previous experimental studies have identified the three lower energy resonances, while only one experimental study reported additionally two core-excited resonances. Previous theoretical scattering studies reported four ${}^{2}B_{1}$ and two ${}^{2}A_{2}$ resonances. In contrast, our calculations have identified four ${}^{2}B_{1}$ and four ²A₂ resonances. Experimental results are based on ETS and their values agree with each other within 0.2 eV. Focusing first on 1p shape resonances, the position for 1^2B_1 is measured to be between 0.6-0.8 eV. 1^2A_2 is measured at 1.2 eV, while 2^2B_1 between 4.5-4.7 eV. Previous scattering calculations predict $1^{2}B_{1}$ to be at 0.7-0.9 eV, $1^{2}A_{2}$ 1.1-1.3 eV and $2^{2}B_{1}$ 5.3-5.8 eV. In these previous theoretical results, the two lower resonances are predicted quite well, while there is a much larger error for 2^2B_1 .

Our EOM-EA-CCSD results predict all resonances to be somewhat higher in energy, with the 1^2B_1 being 0.4-0.6 eV above the experimental values, the 1^2A_2 0.3 eV above experimental values, while the 2^2B_1 has an error of more than 1 eV. Our values for 2^2B_1 are too high, similar to what the scattering methods predicted. Both CASSCF and RASSCF predict the 1^2B_1 and 2^2A_2 resonances to have positions larger than 2 eV, having a very large error. XMS-CASPT2 on the other hand, predicts the first two resonances with similar accuracy as EOM-EA-CCSD, while it does a much better job for 2^2B_1 .

Since the multi-reference methods have difficulty with the balance between the neutral and anion, the position of the first resonance is overestimated by a large value. It is then instructive to also compare the relative energies of the resonances, so in Table VI we have set the position of 1^2B_1 to zero for all results including experimental ones.

The relative positions of the 1^2A_2 resonance with respect to 1^2B_1 are predicted by both EOM-EA-CCSD and multireference methods to be 0.3 eV. This value is close to the previous theoretical values and the experiments by Mathur and Hasted, while the other experiments predict a somewhat higher value. When comparing the relative positions with respect to 1^2B_1 , the most striking effect is how well the multireference methods predict the gap between the two ${}^{2}B_{1}$ resonances, while all other methods drastically overestimate it. The experimental gap is 3.8 - 4 eV, which agrees very well with the multi-reference values. On the other hand, all scattering methods and EOM-EA-CCSD overestimate it by close to 1 eV. This behavior indicates that multi-reference methods are needed for the 2^2B_1 resonance, and this conclusion is in agreement with the mixed character which requires an equivalent description of the different contributing configurations.

The positions for 3^2B_1 and 4^2B_1 resonance align closely with theoretical scattering, while our predictions for 2^2A_2 are lower than Su et al.⁴⁸ Mathur and Hasted⁴² predict two coreexcited resonances in their experiments but they do not assign them. Based on comparison with our values, we assign these two resonances to 4^2B_1 and 4^2A_2 .

Table V compares the widths we calculated with the limited information on widths from the literature. There are no

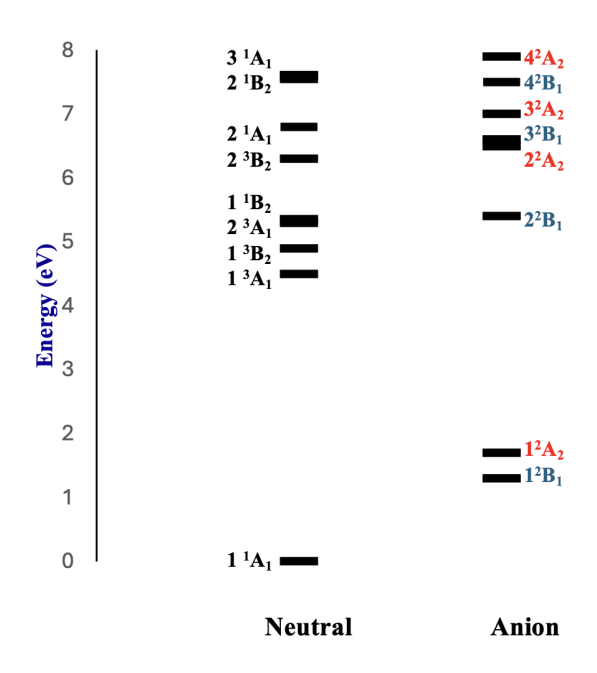


FIG. 9. Energy level diagram showing the energy of neutral excited states and resonances of the anion

experimentally reported widths/lifetimes. However, the fact that vibrational progressions are shown in electron transmission spectra for the first two resonances indicates that their lifetimes most likely are longer than the vibrational period for the progressions (although there are exceptions to this 72), so that means that the widths should also be smaller than the observed frequencies of 0.2 eV. There is no observed structure in the 2^2B_1 resonance, possibly indicating a faster autodetachment lifetime. Our calculated widths agree with these qualitative observations.

The previous widths from scattering calculations agree qualitatively with our results, although their values are somewhat smaller than ours for the first two resonances. The widths for these two resonances predicted with EOM-EA-CCSD are practically the same as those predicted with XMS-CASPT2, and both methods show that the width for 1^2A_2 is larger than the width of 1^2B_1 . Previous scattering calculations predicted the two resonances to have the same widths. The widths calculated for 2^2B_1 are also an order of magnitude larger than those of 1^2B_1 , and all methods predict a width between 0.2-0.5 eV. The multi-reference methods predict values closer to 0.2 eV, which may be a consequence of the mixing between the 1p and 2p-1h characters. The widths we predict for the higher A2 resonances are very small. Very limited previous information on these resonances exists in the literature. Su et al⁴⁸ predict a width of 0.2 eV for 2^2A_2 , a factor of more than three larger than our values. CASSCF/RASSCF and scattering predict a larger width for 4^2B_1 resonance, 0.2-0.4 eV, although XMS-CASPT2 give a smaller width. It should be noted that there are several avoided crossings in this region, and avoided crossings for 3^2B_1 and 4^2B_1 interact. This prohibited us from extracting the positions and widths for 3^2B_1 at

Method/Lit	$1^{2}A_{2}$	$ 2 ^{2}B_{1}$	$ 2 ^2A_2$	$3^{2}B_{1}$	$3^{2}A_{2}$	$4^{2}B_{1}$	$4^{2}A_{2}$
Nenner and Schulz ⁴¹	0.58	3.96	-	-	-	-	-
Modelli and Burrow ⁴³	0.46	3.76	-	-	-	-	-
Szmytkowski et al.44	0.5	3.9	-	-	-	-	-
Mathur and Hasted ⁴²	0.36	3.92	-	-	-	6.48	7.07
Barbosa et al. ⁴⁶	0.43	4.90	-	-	-	-	-
Su et al. ⁴⁸	0.25	4.84	6.12	5.55	-	6.43	-
Sieradzka et al. ⁴⁷	0.40	4.66	-	-	-	-	-
EOM-EA-CCSD	0.30	4.77	-	-	-	-	-
RASSCF	0.31	3.91	5.65	-	6.43	6.47	7.26
CASSCF	0.30	3.73	5.50	-	6.25	6.47	7.06
XMS-CASPT2	0.34	4.1	5.19	5.28	5.68	6.14	6.59

TABLE VI. Comparison of relative positions of selected experimental and theoretical studies (in eV) reported in the literature for Pyridine resonances

the CASSCF/RASSCF levels. It also introduces errors in the calculated widths.

Even though there is no experimental information on the higher energy resonances from the ETS experiments, their presence and importance can be seen in the DEA experiments⁴⁵. Strong signals at 5.3 and 9.0 eV, with a shoulder at 7 eV and another shoulder at 10 eV were observed.

IV. CONCLUSIONS

We investigated four 2B_1 and four 2A_2 resonances below 10 eV in pyridine using the orbital stabilization method with EOM-EA-CCSD, RASSCF, CASSCF, and XMS-CASPT2 theories. Benchmarking different basis sets showed that results plateaued beyond cc-pVTZ+[1p], so we chose this basis set for the calculations. Overall, employing single and multireference methods with GPAs enabled us to identify two shape and six mixed π resonances in pyridine.

Positions from EOM-EA-CCSD were higher than reported literature values, yet widths matched previous theoretical results. The strength of EOM-EA-CCSD lies in balanced treatment of neutral and anionic states, contrasting with multireference methods that require a careful consideration of how to balance the neutral and anion energies. On the other hand, EOM-EA-CCSD cannot describe resonance mixing, so a more useful approach is to use both methods and rely on the advantages of each.

The XMS-CASPT2 method yielded the best results that closely align with experimental data, demonstrating that both dynamical and non-dynamical correlations are important for describing several resonances, including mixed character ones at higher energies. This approach accurately defines all resonances and provide reasonable relative positions.

However, the results from OSM show high uncertainty due to multiple avoided crossings associated with each resonance. It has been shown that this problem is related to different partial widths associated with the different avoided crossings, so it is desirable to be able to extract this information.

Implementation of quadratic and cubic GPA allowed treat-

ment of more complicated and interacting avoided crossings. Combining quadratic and cubic GPAs is recommended to comprehensively capture all existing avoided crossings, including potential unseen ones. Overall, in this work cubic-GPAs yielded results in agreement with quadratic-GPAs.

When using multi-reference methods, an effective strategy to reduce the computational cost is to use RASSCF and include the diffuse orbitals that are needed to describe continuum-like states in the auxiliary space. The values obtained with CASSCF and RASSCF were found to be very similar in our tests, which is expected since correlation is not that important for continuum-like states.

ACKNOWLEDGMENTS

The authors gratefully acknowledge the National Science Foundation for funding this work under Award No. CHE-2303111. Part of the computational work was performed using the Expanse at San Diego Supercomputer Center (SDSC) through allocation CHE140114 from the Advanced Cyberinfrastructure Coordination Ecosystem: Services & Support (ACCESS) program, which is supported by National Science Foundation grant numbers 2138259, 2138286, 2138307, 2137603, and 2138296⁷³

Supplemental Online Material is available. It includes optimized coordinates of the neutral geometry of the pyridine molecule, stabilization plots used for benchmarking, additional information on GPA, and Dyson norms to all reported resonances.

Data Availability Statement: The data that support the findings of this study are available from the corresponding author upon reasonable request.

- ¹I. Baccarelli, I. Bald, F. A. Gianturco, E. Illenberger, and J. Kopyra, Physics Reports **508**, 1 (2011).
- ²J. D. Gorfinkiel and S. Ptasinska, Journal of Physics B: Atomic, Molecular and Optical Physics **50**, 182001 (2017).
- ³M. C. Boyer, N. Rivas, A. A. Tran, C. A. Verish, and C. R. Arumainayagam, Surface Science **652**, 26 (2016).
- ⁴Z. Li, P. Cloutier, L. Sanche, and J. R. Wagner, Journal of the American Chemical Society **132**, 5422 (2010).
- ⁵A. D. Bass and L. Sanche, Radiation Physics and Chemistry **68**, 3 (2003).
- $^6\mathrm{S}.$ Tonzani and C. H. Greene, The Journal of chemical physics 124 (2006).
- ⁷C. R. Arumainayagam, H.-L. Lee, R. B. Nelson, D. R. Haines, and R. P. Gunawardane, Surface Science Reports **65**, 1 (2010).
- ⁸N. J. Mason, B. Nair, S. Jheeta, and E. Szymańska, Faraday Discussions 168, 235 (2014).
- ⁹I. Bald, J. Langer, P. Tegeder, and O. Ingólfsson, International Journal of Mass Spectrometry 277, 4 (2008).
- ¹⁰B. Boudaiffa, P. Cloutier, D. Hunting, M. A. Huels, and L. Sanche, Science 287, 1658 (2000).
- ¹¹R. Barrios, P. Skurski, and J. Simons, The Journal of Physical Chemistry B 106, 7991 (2002).
- ¹²F. Martin, P. D. Burrow, Z. Cai, P. Cloutier, D. Hunting, and L. Sanche, Physical review letters 93, 068101 (2004).
- ¹³L. Sanche, The European Physical Journal D-Atomic, Molecular, Optical and Plasma Physics 35, 367 (2005).
- ¹⁴G. J. Schulz, Reviews of Modern Physics **45**, 423 (1973).
- ¹⁵J. Simons, The Journal of Physical Chemistry A 112, 6401 (2008).
- ¹⁶J. M. Herbert, Reviews in Computational Chemistry Volume 28, 391 (2015).
- ¹⁷N. Moiseyev, P. Certain, and F. Weinhold, Molecular Physics 36, 1613 (1978).

- ¹⁸N. Moiseyev, Physics reports **302**, 212 (1998).
- ¹⁹S. Klaiman and I. Gilary, in *Advances in Quantum Chemistry*, Vol. 63 (Elsevier, 2012) pp. 1–31.
- ²⁰U. Fano, Physical review **124**, 1866 (1961).
- ²¹V. Averbukh and L. S. Cederbaum, The Journal of chemical physics 123 (2005).
- ²²N. Moiseyev, *Non-Hermitian quantum mechanics* (Cambridge University Press, 2011).
- ²³T.-C. Jagau, K. B. Bravaya, and A. I. Krylov, Annual review of physical chemistry 68, 525 (2017).
- ²⁴A. U. Hazi and H. S. Taylor, Physical Review A **1**, 1109 (1970).
- ²⁵H. S. Taylor, Advances in Chemical Physics , 91 (1970).
- ²⁶B. Nestmann and S. Peyerimhoff, Journal of Physics B: Atomic and Molecular Physics 18, 615 (1985).
- ²⁷V. Mandelshtam, T. Ravuri, and H. Taylor, The Journal of chemical physics 101, 8792 (1994).
- ²⁸J. Simons, Annual Review of Physical Chemistry **62**, 107 (2011).
- ²⁹T. C. Thompson and D. G. Truhlar, The Journal of Chemical Physics 76, 1790 (1982).
- ³⁰J. Simons, The Journal of Chemical Physics **75**, 2465 (1981).
- ³¹J.-Y. Chao, M. Falcetta, and K. Jordan, The Journal of chemical physics 93, 1125 (1990).
- ³²C. W. McCurdy and F. Martin, Journal of Physics B: Atomic, Molecular and Optical Physics 37, 917 (2004).
- ³³N. Elander and E. Yarevsky, Physical Review A **57**, 3119 (1998).
- ³⁴C. McCurdy Jr and T. Rescigno, Physical Review Letters **41**, 1364 (1978).
- ³⁵T.-C. Jagau, Chemical Communications **58**, 5205 (2022).
- ³⁶V. Ryaboy, N. Moiseyev, V. Mandelshtam, and H. Taylor, The Journal of chemical physics 101, 5677 (1994).
- ³⁷V. Kukulin and V. Krasnopol'Sky, Journal of Physics A: Mathematical and General 10, L33 (1977).
- ³⁸M. A. Fennimore and S. Matsika, The Journal of Physical Chemistry A 122, 4048 (2018).
- ³⁹A. Landau, I. Haritan, P. R. Kaprálová-Žďánská, and N. Moiseyev, The Journal of Physical Chemistry A 120, 3098 (2016).
- ⁴⁰I. Haritan and N. Moiseyev, The Journal of chemical physics **147** (2017).
- ⁴¹I. Nenner and G. Schulz, The Journal of Chemical Physics **62**, 1747 (1975).
- ⁴²D. Mathur and J. Hasted, Chemical Physics **16**, 347 (1976).
- ⁴³A. Modelli and P. Burrow, Journal of electron spectroscopy and related phenomena 32, 263 (1983).
- ⁴⁴C. Szmytkowski, S. Stefanowska, N. Tańska, B. Żywicka, E. Ptasińska-Denga, and P. Możejko, Molecular Physics 117, 395 (2019).
- ⁴⁵M. Ryszka, E. Alizadeh, Z. Li, and S. Ptasińska, The Journal of Chemical Physics **147**, 094303 (2017).
- ⁴⁶A. S. Barbosa, D. F. Pastega, and M. H. Bettega, Physical Review A 88, 022705 (2013).
- ⁴⁷A. Sieradzka, F. Blanco, M. Fuss, Z. Masin, J. Gorfinkiel, and G. García, The Journal of Physical Chemistry A 118, 6657 (2014).
- ⁴⁸H. Su, X. Cheng, B. Cooper, J. Tennyson, and H. Zhang, The Journal of Chemical Physics 158 (2023).
- ⁴⁹J. Tennyson, Physics Reports **491**, 29 (2010).
- ⁵⁰A. Sieradzka, *Electron attachment to small molecular clusters* (Open University (United Kingdom), 2017).
- ⁵¹M. Thodika, N. Mackouse, and S. Matsika, The Journal of Physical Chemistry A **124**, 9011 (2020).
- ⁵²K. Jordan, Journal of Molecular Spectroscopy **56**, 329 (1975).
- ⁵³L. Yu and J. S.-Y. Chao, Journal of the Chinese Chemical Society 40, 11 (1993).
- ⁵⁴K. Jordan, Chemical Physics **9**, 199 (1975).
- ⁵⁵E. W. Weisstein, https://mathworld. wolfram. com/ (2004).
- ⁵⁶E. W. Weisstein, https://mathworld. wolfram. com/ (2002).
- ⁵⁷J. Bentley and D. M. Chipman, The Journal of chemical physics 86, 3819 (1987).
- ⁵⁸D. E. Muller, Mathematical tables and other aids to computation **10**, 208 (1956).
- ⁵⁹B. P. Pritchard, D. Altarawy, B. Didier, T. D. Gibson, and T. L. Windus, Journal of chemical information and modeling **59**, 4814 (2019).
- ⁶⁰M. Nooijen and R. J. Bartlett, The Journal of chemical physics **102**, 3629 (1995)
- ⁶¹A. I. Krylov, Annu. Rev. Phys. Chem. **59**, 433 (2008).

- ⁶²T.-C. Jagau, The Journal of Chemical Physics **148**, 024104 (2018).
- ⁶³H.-J. Werner, Advances in chemical physics **69**, 1 (2009).
- ⁶⁴H. Lischka, D. Nachtigallova, A. J. A. Aquino, P. G. Szalay, F. Plasser, F. B. C. Machado, and M. Barbatti, Chemical Reviews 118, 7293 (2018).
- ⁶⁵ M. Frisch, G. Trucks, H. schlegel, G. Scuseria, M. Robb, and a. et, "Gaussian 09," (2009).
- ⁶⁶E. Epifanovsky, A. T. Gilbert, X. Feng, J. Lee, Y. Mao, N. Mardirossian, P. Pokhilko, A. F. White, M. P. Coons, A. L. Dempwolff, *et al.*, The Journal of chemical physics 155 (2021).
- ⁶⁷H.-J. Werner, P. J. Knowles, F. R. Manby, J. A. Black, K. Doll, A. Heßelmann, D. Kats, A. Köhn, T. Korona, D. A. Kreplin, *et al.*, The Journal of chemical physics **152** (2020).
- ⁶⁸I. Fdez. Galván, M. Vacher, A. Alavi, C. Angeli, F. Aquilante, J. Autschbach, J. J. Bao, S. I. Bokarev, N. A. Bogdanov, R. K. Carlson, et al., Journal of chemical theory and computation 15, 5925 (2019).
- ⁶⁹M. F. Falcetta, M. C. Fair, S. R. Slimak, K. D. Jordan, and T. Sommerfeld, Physical Chemistry Chemical Physics 25, 31028 (2023).
- ⁷⁰D. Bhattacharya, A. Landau, and N. Moiseyev, Journal of Physical Chemistry Letters 11, 5601 (2020).
- ⁷¹T.-C. Jagau and A. I. Krylov, The Journal of Chemical Physics **144**, 054113 (2016).
- ⁷²K. D. Jordan and P. D. Burrow, Chem. Rev. **87**, 557 (1987).
- ⁷³T. J. Boerner, S. Deems, T. R. Furlani, S. L. Knuth, and J. Towns, in *Practice and Experience in Advanced Research Computing* (2023) pp. 173–176.